

Computational and experimental investigation of a new non equiatomic FCC single-phase Cr₁₅Cu₅Fe₂₀Mn₂₅Ni₃₅ high-entropy alloy

Majid Vaghari, Kamran Dehghani*

Department of Materials and Metallurgical Engineering, Amirkabir University of Technology (Tehran Polytechnic), Hafez Ave., P.O. Box 15875-4413, Tehran, Iran



ARTICLE INFO

Keywords:

High entropy alloys
Density functional theory
Single-phase
Thermal properties
CALPHAD
Cr₁₅Cu₅Fe₂₀Mn₂₅Ni₃₅ HEA

ABSTRACT

The structural, mechanical, and thermal properties of a new non-equiautomic face-centered cubic (FCC) structured high entropy alloy (HEA) were examined computationally using density functional theory (DFT) calculations and validated experimentally. To identify potential single phase HEA candidates, the composition space of the CrCuFeMnNi alloy system, including 1451 alloys, was investigated using the CALculation of PHAs Diagrams (CALPHAD) method and Thermo-Calc software. The CALPHAD approach successfully predicted an FCC single-phase Cr₁₅Cu₅Fe₂₀Mn₂₅Ni₃₅ alloy. Elastic constants and thermal properties of the Cr₁₅Cu₅Fe₂₀Mn₂₅Ni₃₅ HEA were determined through DFT calculations using a 100-atom supercell. To validate the DFT calculations, HEA samples were prepared by the arc melting technique, and X-ray diffraction (XRD) analysis confirmed a single-phase FCC structure.

The DFT calculated elastic constants values satisfied the Born stability conditions for stability of a cubic crystal structure. Pugh's theory indicated that this alloy exhibits ductility and metallic behavior due to its B/G ratio exceeding 1.75 and positive Cauchy pressure. Additionally, Poisson's ratio exceeded 0.26, further confirming its ductile nature. Experimental tests confirmed these findings by measuring bulk modulus, shear modulus, Young's modulus, and Poisson's ratio. The calculated C_V values showed good agreement with experimental data at different temperatures. The linear coefficient of thermal expansion increased rapidly at lower temperatures before becoming linear. Both XRD as well as DFT calculations yielded similar lattice constant results for this HEA. These findings provide insights into various properties of the Cr₁₅Cu₅Fe₂₀Mn₂₅Ni₃₅ HEA, including its structural stability, mechanical behavior and thermal characteristics.

1. Introduction

Since its introduction in 2004, high entropy alloys (HEAs) have garnered significant attention among researchers for designing new alloys with special properties [1]. HEAs, typically consist of four or more elements with equiatomic or nearly equiatomic compositions, where each element's concentration ranging from 5 to 35 at.% [2,3]. These alloys exhibit high strength, toughness, corrosion and wear resistance, thermal stability, and mechanical property retention at cryogenic conditions [4,5].

Given the wide composition space of HEAs, researchers are constantly searching for new candidates with desirable mechanical and physical properties [6,7]. Although property prediction based on HEA composition is still in development, computational studies have emerged as a powerful tool in materials engineering, providing cost and time advantages over experimental research [8]. By employing density

functional theory, first-principles calculations have enabled researchers to investigate the fundamental connection between constituent elements and their characteristics at the atomic and energy levels [9]. These calculations rely solely on quantum mechanical equations and natural constants, facilitating the prediction and exploration of material properties without the need for empirical data [10]. While the physical properties of HEAs have been extensively studied experimentally and theoretically, investigations into the mechanical and thermal properties of HEAs containing elements such as Fe, Co, Cr, Ni, Mn, Al, Cu, Mo, and Ti remain insufficient [11].

In recent years, studies have explored the mechanical and thermal properties of HEAs using first-principles calculations [12–27]. Numerous research studies have utilized first-principles calculations, employing density functional theory, to investigate the stability, thermodynamic properties, and phase stability of CoCrFeMnNi HEAs and their subsystems. Tran et al. [28], focused on phase stability by

* Corresponding author.

E-mail address: dehghani@aut.ac.ir (K. Dehghani).

examining the structural and thermodynamic properties of both equiatomic and non-equiatomic compositions of quinary CoCrFeMnNi HEA. San et al. [29], utilized large supercells with 500 atoms and the VASP package to calculate the electronic structure, interatomic bonding, partial charge distribution, and mechanical properties of CoCrFeMnNi HEA. Another study [30], explored the structural and magnetic properties, as well as thermodynamics and phase stability, of the FeNiCoMn and FeNiCrMn quaternaries, which are medium-entropy alloys derived from the Cantor alloy structure, using density functional theory combined with the quasi-harmonic Debye–Grüneisen approximation and the special-quasirandom structure model. Lobzenko et al. [31], found that the Co-free Cr₂₅Fe₂₅Ni₂₅Mn₂₅ HEA exhibited significant local lattice distortion compared to the well-known Cantor alloy, leading to improved strength and ductility due to the formation of short-range order and non-uniform solid solution states.

In recent years, the development of Co-free HEAs has gained significant attention due to the cost constraints associated with cobalt (Co) and its limited commercial applications. Co-free near-equiatomic CrFe-NiMn HEAs have been successfully synthesized and have demonstrated promising mechanical properties comparable to well-studied Cantor alloys, with some achieving an ultimate tensile strength of up to 500 MPa [32–37]. Copper doping in Co-free HEAs has been the subject of several research studies, although the benefits of copper doping remain inconclusive. Verma et al. demonstrated that the inclusion of copper in the CoCrFeNi alloy led to reduced grain size, increased hardness, and improved wear resistance. Copper also facilitated the formation of a self-lubricating CuO oxide film at elevated temperatures, further enhancing the alloy's tribological properties [38]. In a separate investigation, the AlCoCrFeNiCu_{0.5} HEA exhibited enhanced toughness and corrosion resistance by eliminating copper segregation. The uniform distribution and dispersed nanoscale precipitation of copper in this alloy improved its antifouling and lubricating abilities, making it suitable for applications requiring a combination of mechanical strength, corrosion resistance, and antifouling characteristics [39].

Considering the replacement of the expensive Co element with Cu in Cantor's alloy, the CrCuFeMnNi HEA is formed, which is a quinary equiatomic alloy with both FCC and BCC phases. This alloy exhibits higher yield strength while retaining its formability [40]. Li et al. [41], examined the microstructure of the CrCuFeMnNi HEA for the first time and found that it consists of two major FCC phases and smaller amounts of the body-centered cubic (BCC) phase [40,42–44]. Shabani et al. [45–48], investigated the effects of cold-rolling, heat treatment, and texture on the CrCuFeMnNi HEA, revealing that the as-cast alloy exhibits good mechanical properties, including yield and ultimate tensile strength. However, most studies on the quinary CrCuFeMnNi HEA have focused on the mechanical properties of the equiatomic alloy, while the non-equiatomic HEAs have not been examined extensively. Additionally, no organized study has been conducted to investigate the relationship between composition and properties of the quinary equiatomic or non-equiatomic CrCuFeMnNi HEAs based on the atomic perspective and first-principles calculations. The multiphase nature of the equiatomic CrCuFeMnNi HEA makes it challenging to calculate its elastic constants and electronic properties using the first-principles method, which is more suitable for single-phase alloys [9].

In this investigation, the CALculation of PHase Diagrams (CALPHAD) technique was employed to explore the entire composition space of the non-equiatomic CrCuFeMnNi alloy system, consisting of 1451 alloys, for potential single-phase FCC structured HEA candidates. The X-ray diffraction pattern was utilized to identify peaks corresponding to the single-phase FCC in the selected candidate. Subsequently, first-principles calculations explored the elastic constants and thermodynamic properties of the non-equiatomic quinary HEA with a single-phase FCC structure. These calculations were based on the quasi-harmonic Debye–Grüneisen theory, enabling the examination of temperature-dependent variations in the Debye temperature, linear coefficient of thermal expansion, and heat capacity at constant volume.

The obtained structural, mechanical and thermal properties were validated by comparing them with experimental test results. This research aims to provide guidance for the design and performance prediction of HEA components, which is significant for understanding, optimizing, and applying the novel CrCuFeMnNi HEA system. Such guidance is particularly valuable considering the time-consuming, costly, and complex nature of experimental research due to the need for component regulation.

2. Materials and methods

2.1. Computational details

The CALPHAD approach and the TCHEA2.1 database from Thermo-Calc software were utilized to explore a vast composition space of the CrCuFeMnNi alloy system, which consisted of 1451 alloys (Supplementary Information-I). Thermodynamic calculations were conducted in the temperature range of 500–1900 K with a step temperature of 10 K in a Linux environment. Subsequently, the results were screened to identify potential single-phase HEA candidates. More detailed information regarding the high-throughput Thermo-Calc route and thermodynamic calculations can be found in Ref. [49].

The plane-wave pseudopotential approach, implemented in the quantum-espresso package [50], was utilized for density functional theory (DFT) calculations based on Density Functional Theory. The exchange-correlation function was described using the Generalized Gradient Approximation (GGA) of the Perdew Burke Ernzerhof (PBE) scheme [51]. The kinetic energy cut-off was set to 40 Rydberg (Ry), and the charge-density cut-off was chosen as 8 times the kinetic energy cut-off. Brillouin zone integrations were performed using an 8 × 2 × 2 k-points mesh, and a Methfessel-Paxton scheme with a smearing value of 0.01 Ry was applied. Elastic and thermodynamic properties were computed using the thermo_pw package. To construct a random structure of FCC supercell with 100 atoms (Fig. 1), the Alloy Theoretic Automated Toolkit (ATAT) code and the Knuth shuffle model [52] were employed. The convergence test for the randomly distributed supercell is described in detail in Refs. [53–55]. The computational efficiency of this supercell with 100 atoms has been confirmed to yield accurate results for the distribution of elements in complex randomly alloyed structures in Refs. [24,53].

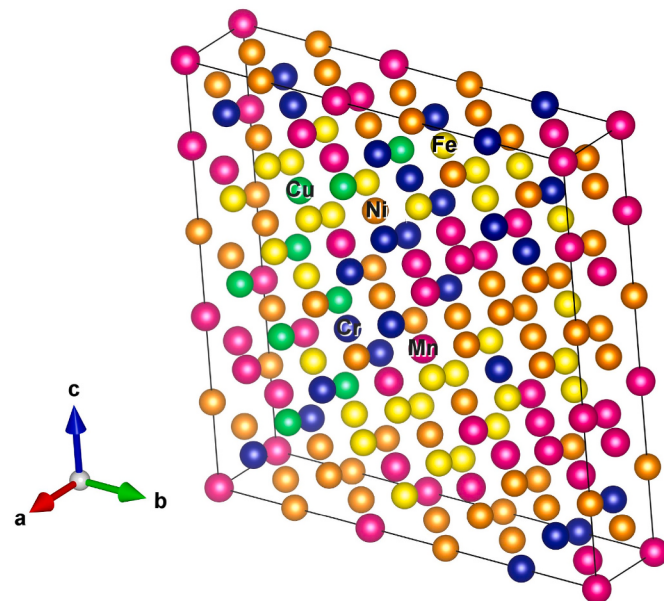


Fig. 1. Schematic visualization of the randomly distributed 100-atom supercell of Cr₁₅Cu₅Fe₂₀Mn₂₅Ni₃₅ HEA.

The mechanical properties of the Cr₁₅Cu₅Fe₂₀Mn₂₅Ni₃₅ HEA were computed using the Voigt-Reuss-Hill approximation [56,57] after calculating the elastic constants. The bulk modulus (B), shear modulus (G), Young's modulus (E), and Poisson ratio (ν) were calculated using the following equations:

$$B = \frac{1}{3}(C_{11} + 2C_{12}) \quad (1)$$

$$G = \frac{1}{2}(G_{\text{Voight}} + 2G_{\text{Reuss}}) \quad (2)$$

$$E = \frac{9BG}{3B + G} \quad (3)$$

$$\nu = \frac{3B - 2G}{2(3B + G)} \quad (4)$$

Where G_{Voight} and G_{Reuss} are defined as:

$$G_{\text{Voight}} = \frac{1}{5}(C_{11} - C_{12} + 3C_{44}) \quad (5)$$

$$G_{\text{Reuss}} = \frac{5}{4(S_{11} - S_{12}) + 3S_{44}} \quad (6)$$

C and S represent the elastic constant and compliance matrix, respectively. Thermodynamic properties calculations are based on the Debye theory [58]. The Debye temperature (θ_D) was computed by using the formula of the mean sound velocity (V_m) as follows:

$$\theta_D = \frac{\hbar}{K_B} \left(\frac{6\pi^2 q}{V_0} \right)^{\frac{1}{3}} V_m \quad (7)$$

The Grüneisen [56] constant (γ_G), was initially set to 2, and then the γ_G was derived from the pressure–volume equation by Mayer et al. [59]. Here, V₀ is the equilibrium volume and B is bulk modulus and q represents the number of atoms in the unit cell, V₀ is its volume, \hbar and K_B are the Planks and Boltzmann constant respectively.

The linear coefficient of thermal expansion, α_L , and the heat capacity at constant volume, C_V, as functions of temperature, T, are estimated as:

$$\alpha_L(T) = \frac{1}{3}\gamma_G \frac{C_V(T)}{BV_0} \quad (8)$$

$$C_V(T) = pqk_B \left(\frac{T}{\theta_D} \right)^3 \int_0^{\infty} \frac{x^4 \exp(x)}{(\exp(x) - 1)^2} dx \quad (9)$$

2.2. Experimental details

The Cr₁₅Cu₅Fe₂₀Mn₂₅Ni₃₅ samples prepared with the arc melting from 99.9 % pure elements. The melting procedure was carried out under an inert Ar gas atmosphere in the crucible. To ensure good chemical homogeneity, the ingots were remelted at least 5 times.

Cylindrical specimens (D = 4 mm and L = 10 mm) were prepared by EDM (electric discharge machining) for measuring the linear coefficient of thermal expansion, and the tests were conducted following the ASTM E228-11 standard [60]. The tests were conducted in the temperature range of 273 K–1000 K with a heating rate of 2 K/min. The heat capacity at constant volume of the samples was measured following the ASTM E1269-1 standard [61].

Tensile test samples were prepared using electrical discharge machining (EDM) for the examination of mechanical properties. The gauge width was 2.5 mm, and the length was 6.4 mm. Tensile tests were performed using tensile testing equipment (H25KS, UK). The modulus of elasticity was measured with the ASTM E1876-01 standard test method [62]. Plates with dimensions of 30 × 12 × 1.5 mm³ and beams with dimensions of 30 × 5 × 1 mm³ were tested in torsion and bending modes, respectively. Plates with dimensions of 25 × 12 × 1.5 mm³ and

beams with dimensions of 25 × 5 × 1 mm³ were electric discharge machined and tested in torsion and bending modes, respectively. The shear modulus was determined by analyzing the torsional deformation of plates. The torsional resonance frequency f, was determined by sweeping the excitation frequency using a network analyzer within the kHz frequency range. The shear modulus was subsequently calculated according to:

$$G = \rho f^2 \frac{(t^2 + b^2)L^2}{\left(1 - \frac{t}{\sqrt{3}b}\right)t^2} \quad (10)$$

$$E = 0.9465\rho f^2 \left(\frac{L^4}{t^2} \right) h \quad (11)$$

Where f is the bending resonance frequency, ν is Poisson's ratio, ρ is density, and m, b, L and t are the beam weight, beam width, length and thickness, respectively [63]. The h is a correction factor and can be found in Ref. [64].

The microstructure and chemical compositions of the samples were examined using a field emission scanning electron microscope (TESCAN Mira 3 XMU, TESCAN, Brno, Czech Republic) equipped with a secondary electron (SE) detector and an energy dispersive spectroscopy (EDS) detector. The crystal structure of the sample was analyzed using X-ray diffraction (XRD) with a PANalytical X'Pert PRO diffractometer equipped with Cu-Kα radiation. Before microstructure examination, the samples were etched using the Marble etchant (composed of 10 % HCl and 5 % HNO₃, with the remainder being methanol).

3. Results and discussion

3.1. Thermodynamic calculations

The isothermal section of a pseudo-ternary diagram for the 1451 CrCuFeMnNi alloys at various temperatures is presented in Fig. 2. Regions of interest within the composition space are highlighted, and the evolution of phases with temperature is illustrated. Notably, at 900 K (as shown in Fig. 2-a), single-phase FCC alloys are not observed across the entire composition space. However, as the temperature is increased to 1200 K (as depicted in Fig. 2-d), a significant expansion of the single-phase FCC region is observed, indicated by the red area.

Upon analysis of this region, 27 quinary CrCuFeMnNi alloys that consistently exhibited a single-phase face-centered cubic (FCC) structure over a wide temperature range were identified. These alloys are summarized in Table 1, which provides their respective compositions and the temperature ranges where the FCC phase fraction equals 1. Of particular interest is the alloy Cr₁₅Cu₅Fe₂₀Mn₂₅Ni₃₅, which was found to demonstrate the widest temperature range of this behavior.

It can be observed from Table 1, that the Cr₁₅Cu₅Fe₂₀Mn₂₅Ni₃₅ HEA possesses the lowest amount of Cu compared to other choices.

Consequently, this alloy, Cr₁₅Cu₅Fe₂₀Mn₂₅Ni₃₅, was selected for further experimental examination. This choice was made to minimize the presence of a Cu-rich FCC phase, which is a common issue in Cu-containing HEAs. Copper atoms tend to segregate in the interdendritic space and/or at grain boundaries during crystallization, leading to the formation of pure copper precipitates. These precipitates can adversely affect the hardness, corrosion resistance, and wear resistance of multi-component alloys [38,65–67].

3.2. Structural properties

Based on the CALPHAD technique, a non-equiautomatic FCC structured single-phase HEA candidate, denoted as Cr₁₅Cu₅Fe₂₀Mn₂₅Ni₃₅, was successfully predicted across a wide temperature range. The calculated equilibrium phase diagram of the Cr₁₅Cu₅Fe₂₀Mn₂₅Ni₃₅ alloy, generated using Thermo-Calc software, is presented in Fig. 3, displaying the phase

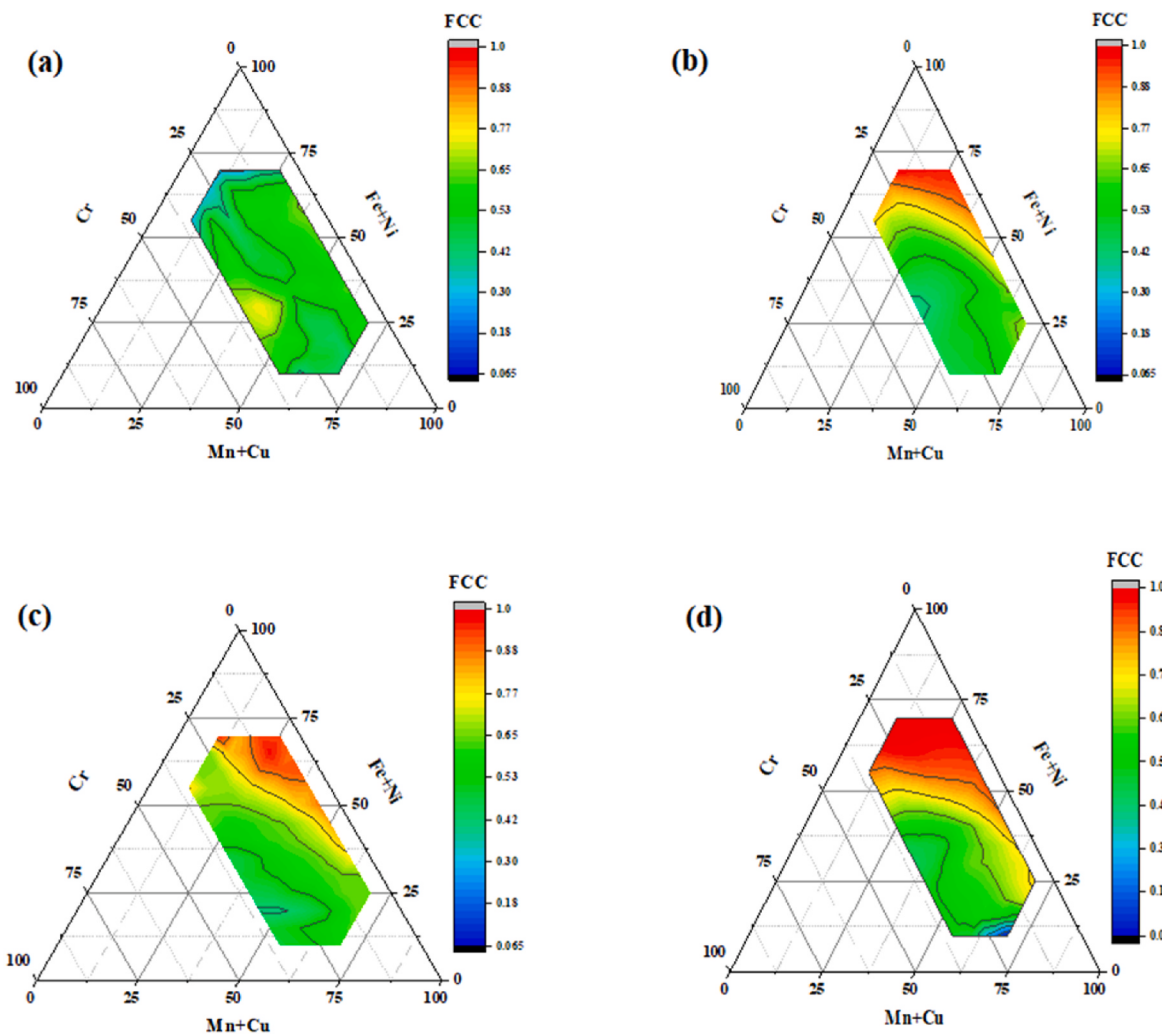


Fig. 2. Isothermal section of a pseudo ternary diagram of non-equiautomic CrCuFeMnNi alloys at (a) 900 K (b) 1000 K (c) 1100 K (d) 1200 K.

diagram of the Cr₁₅Cu₅Fe₂₀Mn₂₅Ni₃₅ HEA in the temperature range of 500–1900 K. The XRD analysis of the Cr₁₅Cu₅Fe₂₀Mn₂₅Ni₃₅ alloy also exhibited distinct peaks corresponding to a FCC single-phase, as depicted in Fig. 4.

Therefore, the XRD results validate the Thermo-Calc prediction, confirming that Cr₁₅Cu₅Fe₂₀Mn₂₅Ni₃₅ is indeed a single-phase FCC structured HEA.

Other researchers have shown that in the equiautomic CrCuFeMnNi high-entropy alloy, the XRD pattern reveals the presence of two FCC phases, in addition to a BCC phase. Similarly, in the case of the non-equiautomic CrCu_xFeMnNi alloys, both FCC and BCC phases were confirmed to be present [40,42,46,48].

3.3. Mechanical properties

The mechanical properties of the Cr₁₅Cu₅Fe₂₀Mn₂₅Ni₃₅ HEA were determined through a combination of Density Functional Theory (DFT) calculations at zero pressure and zero Kelvin temperature and experimental tests, as summarized in Table 2.

Based on DFT calculations, the elastic constants of the Cr₁₅Cu₅Fe₂₀Mn₂₅Ni₃₅ HEA were determined. Table 2 presents the calculated and experimental mechanical properties and elastic constants of the alloy. According to the Born stability conditions, a cubic crystal structure is stable when (C₄₄ > 0, C₁₁>|C₁₂|, and C₁₁+2C₁₂ > 0) [17,24]. The elastic constants calculated using DFT indicate that the Cr₁₅Cu₅Fe₂₀Mn₂₅Ni₃₅ HEA is elastically stable, satisfying all the stability

conditions.

Pugh's theory [21,68] suggests that the B/G ratio determines ductility, and the sign of the Cauchy pressure (C₁₁– C₄₄) [69] is used to study the material's plastic properties. If the B/G ratio is greater than 1.75 and the Cauchy pressure is positive, the material exhibits ductility and metallic behavior [21]. The calculations show that the B/G ratio for the Cr₁₅Cu₅Fe₂₀Mn₂₅Ni₃₅ HEA is greater than 1.75, and the Cauchy pressure is positive, confirming its ductile and metallic nature. Furthermore, for ductile materials, Poisson's ratio should exceed 0.26 [67–69]. The estimated value of Poisson's ratio ν given in Table 2, which is 0.31, further confirms the alloy's ductile nature.

Kim et al. employed DFT to assess mechanical properties of FCC Al_{0.3}CoCrFeNi HEA. They found the shear modulus to be ~85 GPa, 5 % higher than the experimental value (81 GPa), and the Young's modulus to be ~195 GPa, deviating by 9 % from the experimental value (215 GPa). They also determined the Poisson ratio (ν) as ~0.29 and the B/G ratio as ~2.07 [70].

Experimental tests were conducted to determine the elastic properties, including bulk modulus, shear modulus, Young's modulus, and Poisson's ratio, are also shown in Table 2. Fig. 5 compares the calculated and experimental values of the bulk modulus, shear modulus, and Young's modulus. The comparison demonstrates the excellent agreement between the DFT model and experimental results. It is important to note that the measurement of Young's modulus, shear modulus, and Poisson's ratio followed the ASTM E1876-01 standard test method. Proper specimen geometry, dimensions, and surface finish are critical

Table 1
Predicted single-phase FCC alloys.

#	Composition (CrCuFeMnNi)	Temperature Range (K)
1	Cr ₁₅ Cu ₅ Fe ₂₀ Mn ₂₅ Ni ₃₅	1100–1440
2	Cr ₁₀ Cu ₁₅ Fe ₅ Mn ₃₅ Ni ₃₅	1030–1320
3	Cr ₁₀ Cu ₁₅ Fe ₁₀ Mn ₃₀ Ni ₃₅	1060–1350
4	Cr ₁₅ Cu ₁₀ Fe ₁₅ Mn ₂₅ Ni ₃₅	1110–1400
5	Cr ₅ Cu ₃₀ Fe ₅ Mn ₃₀ Ni ₃₀	1050–1310
6	Cr ₅ Cu ₂₅ Fe ₅ Mn ₃₅ Ni ₃₀	1040–1290
7	Cr ₁₀ Cu ₂₀ Fe ₅ Mn ₃₀ Ni ₃₅	1090–1330
8	Cr ₁₅ Cu ₁₀ Fe ₁₅ Mn ₃₀ Ni ₃₀	1180–1370
9	Cr ₁₅ Cu ₁₅ Fe ₁₀ Mn ₂₅ Ni ₃₅	1170–1360
10	Cr ₁₀ Cu ₁₅ Fe ₁₀ Mn ₃₅ Ni ₃₀	1140–1320
11	Cr ₅ Cu ₃₅ Fe ₁₀ Mn ₂₅ Ni ₂₅	1160–1320
12	Cr ₅ Cu ₃₀ Fe ₅ Mn ₃₅ Ni ₂₅	1130–1280
13	Cr ₅ Cu ₃₅ Fe ₅ Mn ₃₀ Ni ₂₅	1140–1290
14	Cr ₁₀ Cu ₂₀ Fe ₅ Mn ₃₅ Ni ₃₀	1160–1300
15	Cr ₂₀ Cu ₁₀ Fe ₁₀ Mn ₂₅ Ni ₃₅	1240–1380
16	Cr ₅ Cu ₃₅ Fe ₁₅ Mn ₂₀ Ni ₂₅	1220–1350
17	Cr ₁₀ Cu ₃₅ Fe ₁₀ Mn ₁₀ Ni ₃₅	1300–1400
18	Cr ₁₅ Cu ₁₅ Fe ₁₀ Mn ₃₀ Ni ₃₀	1240–1330
19	Cr ₁₀ Cu ₂₀ Fe ₁₀ Mn ₃₅ Ni ₂₅	1220–1300
20	Cr ₅ Cu ₃₅ Fe ₂₀ Mn ₁₅ Ni ₂₅	1310–1360
21	Cr ₁₀ Cu ₂₅ Fe ₁₀ Mn ₃₀ Ni ₂₅	1250–1300
22	Cr ₁₀ Cu ₃₅ Fe ₁₀ Mn ₁₅ Ni ₃₀	1310–1360
23	Cr ₅ Cu ₃₀ Fe ₁₀ Mn ₃₅ Ni ₂₀	1230–1270
24	Cr ₅ Cu ₃₅ Fe ₅ Mn ₃₅ Ni ₂₀	1210–1250
25	Cr ₅ Cu ₃₅ Fe ₁₀ Mn ₃₀ Ni ₂₀	1250–1280
26	Cr ₅ Cu ₃₅ Fe ₁₅ Mn ₂₅ Ni ₂₀	1270–1300
27	Cr ₁₅ Cu ₁₅ Fe ₅ Mn ₃₅ Ni ₃₀	1280–1300

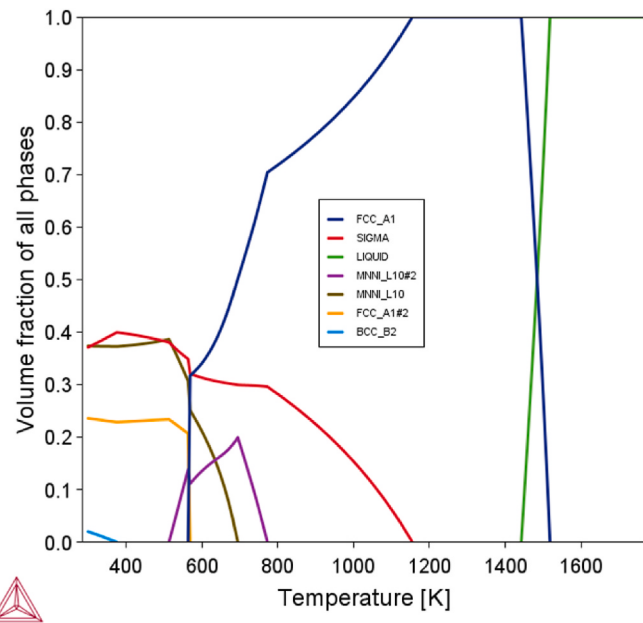


Fig. 3. Calculated equilibrium phase diagram of the Cr₁₅Cu₅Fe₂₀Mn₂₅Ni₃₅ HEA.

factors that can affect test results and introduce errors [71].

The Young's modulus of the CoCrFeMnNi High Entropy Alloy (HEA) was predicted to be 267 GPa using Density Functional Theory (DFT), representing a 32 % deviation from the experimental value of 202 GPa. Similarly, for the CoCrFeNi HEA, DFT predicted a Young's modulus of 242 GPa, deviating by 13 % from the experimental value of 215 GPa [72–75]. However, in this study, The DFT-predicted Young's modulus for the Cr₁₅Cu₅Fe₂₀Mn₂₅Ni₃₅ HEA is slightly higher, approximately 6 %, than the experimental value.

The tensile test curve of the as-cast Cr₁₅Cu₅Fe₂₀Mn₂₅Ni₃₅ HEA at room temperature is illustrated in Fig. 6. The ultimate tensile strength (UTS), yield strength (YS), and elongation values are 475 MPa, 220 MPa,

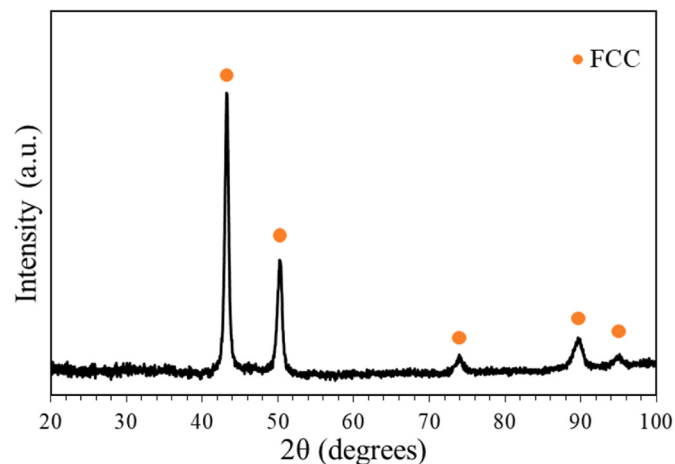


Fig. 4. XRD pattern for the as-cast Cr₁₅Cu₅Fe₂₀Mn₂₅Ni₃₅ HEA.

and 22 %, respectively (Table 3). The alloy exhibits medium strength and good ductility compared to the as-cast equiatomic CrCuFeMnNi HEA, which reported UTS of 950 MPa and an elongation of 14 % [48]. The presence of a continuous ductile matrix is the primary reason for its ductile behavior [48]. On the other hand, the combination of FCC and BCC phases in the equiatomic alloys made it more strength and lower ductility vs as-cast Cr₁₅Cu₅Fe₂₀Mn₂₅Ni₃₅ HEA.

As it can be seen in Table 4, the Cr₁₅Cu₅Fe₂₀Mn₂₅Ni₃₅ HEA demonstrates a combination of favorable mechanical properties, with an ultimate tensile strength of 475 MPa and an elongation of 22 %. However, alloys with higher ultimate tensile strengths often exhibit lower ductility, which is crucial in applications requiring a balance between strength and deformability. The Cr₁₅Cu₅Fe₂₀Mn₂₅Ni₃₅ HEA offers a compelling combination of strength and ductility, positioning it as a promising candidate for various engineering applications.

Furthermore, the focus of this research is on the development of a Co-free HEA with an FCC structure, addressing cost constraints and broadening the range of available materials in this category. This unique aspect of the Cr₁₅Cu₅Fe₂₀Mn₂₅Ni₃₅ HEA composition, coupled with its competitive mechanical properties, adds to its significance in the field of high-entropy alloys.

3.4. Thermal properties

The thermodynamic properties of the Cr₁₅Cu₅Fe₂₀Mn₂₅Ni₃₅ HEA were calculated using the Debye theory [58]. Table 5 presents the calculated values of the heat capacity at constant volume C_V (J/K/mol) and the linear coefficient of thermal expansion α_L ($10^{-6}/\text{K}$). Additionally, the calculated mean sound velocity, Debye temperature, and Grüneisen parameter of the Cr₁₅Cu₅Fe₂₀Mn₂₅Ni₃₅ alloy were determined as 3010 m/s, 350.1 K, and 1.83, respectively.

The literature review has revealed that DFT-calculated values of the heat capacity at constant volume and the linear coefficient of thermal expansion exhibit similar trends to the results obtained in this study. Specifically, the values of α_L and C_V increase rapidly at lower temperatures and then gradually become linear [15,17,20,24].

The measurement of heat capacity at constant volume (C_V) and the linear coefficient of thermal expansion (α_L) followed the ASTM E1269-1 and ASTM E228-11 standard tests, respectively. Fig. 7-(a) presents a graph plotting the temperature against the calculated and experimental C_V values for the Cr₁₅Cu₅Fe₂₀Mn₂₅Ni₃₅ HEA. The C_V value for the alloy exhibits a rise at lower temperatures (250–600 K) and becomes linear at higher temperatures above 600 K. The results of the DFT calculations are in good agreement with the experimental data. Fig. 7-(b) shows the calculated and experimental values of the linear coefficient of thermal expansion (α_L) as a function of temperature for the

Table 2

DFT calculations and experimental results for mechanical properties of $\text{Cr}_{15}\text{Cu}_5\text{Fe}_{20}\text{Mn}_{25}\text{Ni}_{35}$ HEA.

	C_{11} (GPa)	C_{12} (GPa)	C_{44} (GPa)	$C_{11}-C_{44}$ (GPa)	B (GPa)	G (GPa)	E (GPa)	ν	B/G	a (\AA)	ρ (g.cm ⁻³)
DFT	311	191	150	161	232	97	255	0.31	2.39	3.49	8.66
Experimental	–	–	–	–	220	91	240	0.32	2.42	3.62	–

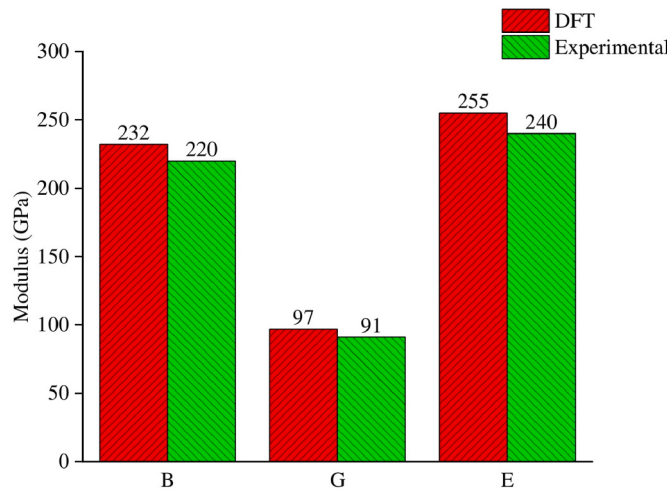


Fig. 5. The calculated and experimental bulk modulus (B), shear modulus (G), and Young's modulus (E) for $\text{Cr}_{15}\text{Cu}_5\text{Fe}_{20}\text{Mn}_{25}\text{Ni}_{35}$ HEA.

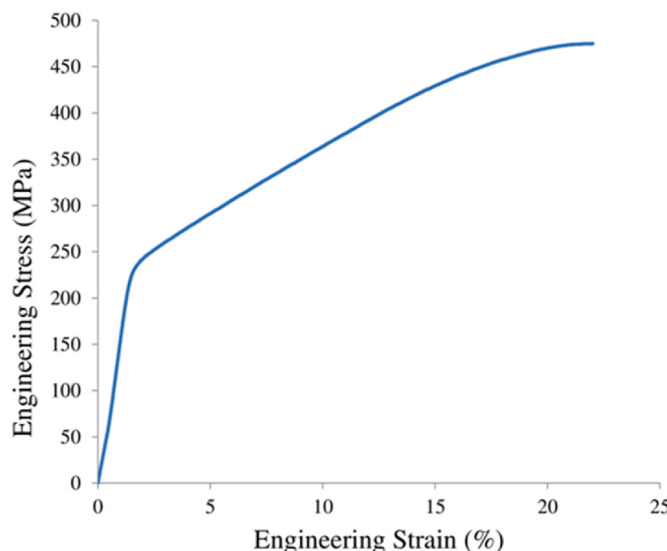


Fig. 6. Engineering stress-strain curve of as-cast $\text{Cr}_{15}\text{Cu}_5\text{Fe}_{20}\text{Mn}_{25}\text{Ni}_{35}$ HEA under tension.

Table 3

Tensile properties of $\text{Cr}_{15}\text{Cu}_5\text{Fe}_{20}\text{Mn}_{25}\text{Ni}_{35}$ HEA measured at room temperature.

Alloy	Phase	YS (MPa)	UTS (MPa)	Elongation (%)
$\text{Cr}_{15}\text{Cu}_5\text{Fe}_{20}\text{Mn}_{25}\text{Ni}_{35}$	FCC	220	475	22

$\text{Cr}_{15}\text{Cu}_5\text{Fe}_{20}\text{Mn}_{25}\text{Ni}_{35}$ alloy. The value of α_L increases rapidly at temperatures below 500 K and then gradually becomes linear. The experimental test results follow a similar trend.

Alongside the mechanical and thermal properties, the lattice constant and microstructure of the $\text{Cr}_{15}\text{Cu}_5\text{Fe}_{20}\text{Mn}_{25}\text{Ni}_{35}$ HEA were examined as follows:

Table 4

Tensile properties of some single-phase FCC HEAs [76].

Alloy	UTS (MPa)	Elongation (%)
CoCrNi	860	60
CoMnNi	653	38
FeMnNi	602	36
CoCrFeNi	708	39
CoGrMnNi	694	44
CoFeMnNi	550	41
CoCuFeNi	480	15
CoCuFeNiSn _{0.02}	548	17
CoCuFeMnNi	478	14
CoCuFeMnNiSn _{0.03}	465	18

Table 5

Calculated C_V and α_L for $\text{Cr}_{15}\text{Cu}_5\text{Fe}_{20}\text{Mn}_{25}\text{Ni}_{35}$ HEA.

Property	Temperature (K)	DFT	Experimental
C_V (J/K/mol)	100	166.80	163.12
	300	429.02	423.05
	850	489.44	487.03
α_L ($10^{-6}/\text{K}$)	100	3.25	3.23
	300	8.36	8.30
	850	9.53	9.49

The lattice constant of the $\text{Cr}_{15}\text{Cu}_5\text{Fe}_{20}\text{Mn}_{25}\text{Ni}_{35}$ HEA was determined using Density Functional Theory (DFT) calculations, yielding a value of 3.49 Å. In contrast, experimental measurements obtained via X-ray Diffraction (XRD) revealed a slightly larger lattice constant of 3.62 Å. This observed discrepancy is consistent with prior research findings [42,47,48,74], which corroborate the XRD-derived lattice constant.

The 4 % difference between the DFT-calculated lattice constant (3.49 Å) and the experimental XRD value (3.62 Å) can be attributed to various factors, including the inherent complexity of the alloy system, temperature variations (DFT calculations conducted at absolute zero vs. XRD measurements at 300 K), and minor experimental errors.

Fig. 8- (a) and (b) present the dendritic structure of the $\text{Cr}_{15}\text{Cu}_5\text{Fe}_{20}\text{Mn}_{25}\text{Ni}_{35}$ HEA. The results of the energy-dispersive spectroscopy (EDS) composition analysis for the alloy (red area in **Fig. 8-** (b)) are presented in **Table 6**, revealing an even distribution of elements throughout the microstructure.

As it can be seen from **Fig. 8-** (b), The EDS analysis was conducted on the dendritic region of the microstructure.

Finally, the fracture behavior of the $\text{Cr}_{15}\text{Cu}_5\text{Fe}_{20}\text{Mn}_{25}\text{Ni}_{35}$ HEA was examined. The tensile test fracture surface of the as-cast $\text{Cr}_{15}\text{Cu}_5\text{Fe}_{20}\text{Mn}_{25}\text{Ni}_{35}$ HEA exhibited ductile behavior, indicated by the presence of deep, equiaxed dimples on the fracture surface, as shown in **Fig. 9**. This indicates significant plastic deformation and slow tearing of the metal as cracks propagate. Examination of the sample surface revealed numerous equiaxed dimples on the fracture surface. In contrast, brittle fractures lack dimple formation and display smooth surfaces with minimal plastic deformation and cleavage facets [77,78].

4. Conclusions

In this study, a non-equiautomic $\text{Cr}_{15}\text{Cu}_5\text{Fe}_{20}\text{Mn}_{25}\text{Ni}_{35}$ FCC structured single-phase HEA was successfully designed using the CALPHAD approach. The alloy's structural, mechanical, thermal and microstructural properties were systematically investigated through a combination

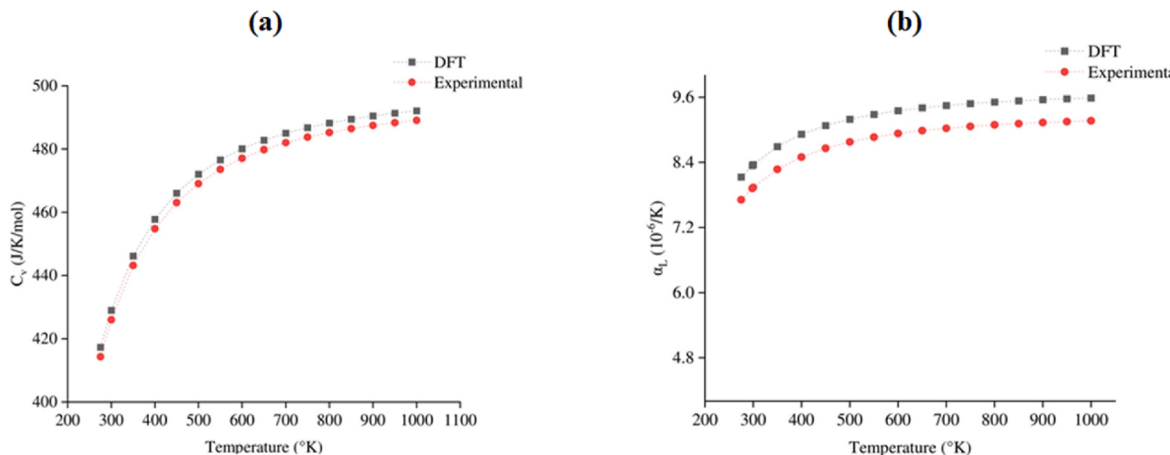


Fig. 7. (a) The calculated and experimental vibrational heat capacity at constant volume (C_V) vs temperature and (b) The calculated and experimental linear coefficient of thermal expansion (α_l) vs temperature for the $\text{Cr}_{15}\text{Cu}_5\text{Fe}_{20}\text{Mn}_{25}\text{Ni}_{35}$ HEA.

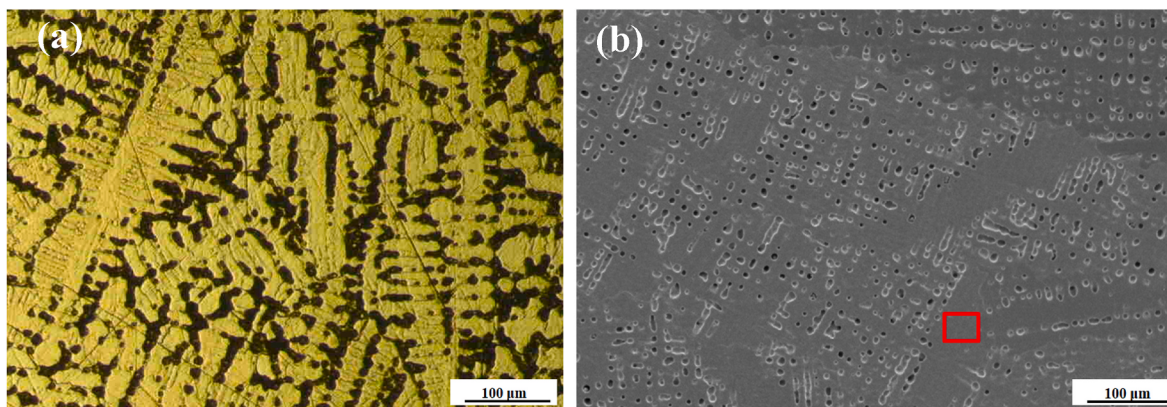


Fig. 8. (a) Optical and (b) SEM micrographs of the as-cast $\text{Cr}_{15}\text{Cu}_5\text{Fe}_{20}\text{Mn}_{25}\text{Ni}_{35}$ high entropy alloy.

Table 6

The EDS composition analysis results for the $\text{Cr}_{15}\text{Cu}_5\text{Fe}_{20}\text{Mn}_{25}\text{Ni}_{35}$ alloy.

Elements	Composition (at.%)
Cr	14.3 ± 0.8
Cu	3.7 ± 0.6
Fe	22.1 ± 1.1
Mn	23.4 ± 0.5
Ni	32.4 ± 0.7

of DFT calculations, experimental measurements and microstructure analysis.

The CALPHAD method predicted the formation of a stable single-phase FCC structure, a prediction that was subsequently validated through XRD analysis. DFT calculations yielded a lattice constant of 3.49 Å, slightly deviating from the experimental value of 3.62 Å determined through XRD analysis. This difference can be attributed to the fact that DFT calculations were conducted at absolute zero, whereas XRD measurements were performed at 300 K. The mechanical properties of ultimate tensile strength, yield strength, and elongation were experimentally determined to be 475 MPa, 220 MPa, and 22 % respectively, indicating a good combination of strength and ductility. The bulk modulus, shear modulus, Young's modulus and Poisson's ratio obtained experimentally also matched well with DFT predictions. The thermal properties including heat capacity and thermal expansion coefficient followed expected increasing trends with temperature. The DFT

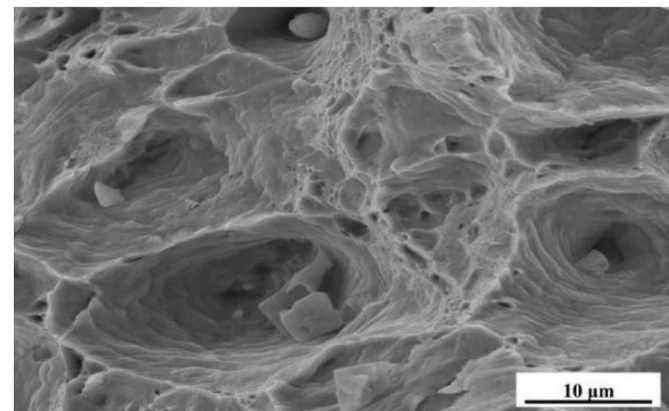


Fig. 9. SEM images of the fracture surface of as-cast $\text{Cr}_{15}\text{Cu}_5\text{Fe}_{20}\text{Mn}_{25}\text{Ni}_{35}$ HEA after the tensile test.

predicted values were in good agreement with experimental measurements. The alloy exhibited a dendritic microstructure with an even distribution of elements, as revealed by SEM/EDS analysis. A high density of dimples in the tensile fracture surface confirmed the significant ductility of this alloy. In summary, this study validated that DFT calculations can provide reasonably accurate predictions of properties for new complex HEAs. By combining computational and experimental techniques, a robust approach to accelerated alloy design and

optimization can be developed. The Cr₁₅Cu₅Fe₂₀Mn₂₅Ni₃₅ HEA showed promising strength, ductility and stability, demonstrating its potential as an advanced structural material.

CRediT authorship contribution statement

Majid Vaghari: experimental design, Formal analysis. **Kamran Dehghani:** Conceptualization, Methodology, Formal analysis.

Declaration of competing interest

The authors declare that they have no known competing financial interests or personal relationships that could have appeared to influence the work reported in this paper.

Data availability

Data will be made available on request.

Appendix A. Supplementary data

Supplementary data to this article can be found online at <https://doi.org/10.1016/j.physb.2023.415413>.

References

- [1] A. Kumar, A. Singh, A. Suhane, Mechanically alloyed high entropy alloys: existing challenges and opportunities, *J. Mater. Res. Technol.* 17 (Mar. 2022) 2431–2456, <https://doi.org/10.1016/J.JMRT.2022.01.141>.
- [2] S. Gorsse, J.P. Couzinié, D.B. Miracle, From high-entropy alloys to complex concentrated alloys, *Compt. Rendus Phys.* 19 (8) (Dec. 2018) 721–736, <https://doi.org/10.1016/J.CRHY.2018.09.004>.
- [3] H.J. Park, Y.S. Kim, S.C. Mun, S.H. Hong, W.M. Wang, K.B. Kim, Designing of Fe-containing (Ti₃₃Zr₃₃Hf₃₃)-(Ni₅₀Cu₅₀) high entropy alloys developed by equiatomic substitution: phase evolution and mechanical properties, *J. Mater. Res. Technol.* 9 (4) (Jul. 2020) 7732–7739, <https://doi.org/10.1016/J.JMRT.2020.05.071>.
- [4] A. Karati, K. Guruvidyathri, V.S. Hariharan, B.S. Murty, Thermal stability of AlCoFeMnNi high-entropy alloy, *Scripta Mater.* 162 (Mar. 2019) 465–467, <https://doi.org/10.1016/j.scriptamat.2018.12.017>.
- [5] Z. Lyu, X. Fan, C. Lee, S.Y. Wang, R. Feng, P.K. Liaw, Fundamental understanding of mechanical behavior of high-entropy alloys at low temperatures: a review, *J. Mater. Res.* 33 (19) (Oct. 2018) 2998–3010, <https://doi.org/10.1557/JMR.2018.273>.
- [6] M.C. Gao, P.K. Liaw, J.W. Yeh, Y. Zhang, High-entropy Alloys: Fundamentals and Applications, Springer International Publishing, 2016, <https://doi.org/10.1007/978-3-319-27013-5>.
- [7] D.B. Miracle, O.N. Senkov, A critical review of high entropy alloys and related concepts, *Acta Mater.* 122 (Jan. 2017) 448–511, <https://doi.org/10.1016/j.actamat.2016.08.081>.
- [8] B. Hendrickson, Computational science: emerging opportunities and challenges, *J. Phys. Conf. Ser.* 180 (1) (2009), <https://doi.org/10.1088/1742-6596/180/1/012013>.
- [9] Z.S. Nong, J.C. Zhu, R. Da Zhao, Prediction of structure and elastic properties of AlCrFeNiTi system high entropy alloys, *Intermetallics* 86 (Jul. 2017) 134–146, <https://doi.org/10.1016/J.INTERMET.2017.03.014>.
- [10] Y. Ikeda, B. Grabowski, F. Körmann, *Ab Initio Phase Stabilities and Mechanical Properties of Multicomponent Alloys: A Comprehensive Review for High Entropy Alloys and Compositionally Complex Alloys*, vol. 147, Elsevier Inc., 2019, pp. 464–511.
- [11] Y. Liu, Z. Wang, H. Xiao, G. Chen, T. Fan, L. Ma, Mechanical properties of CrFeCoNiCu_x (0 ≤ x ≤ 0.3) HEAs from first-principles calculations, *RSC Adv.* 10 (68) (Nov. 2020) 41324–41331, <https://doi.org/10.1039/DORA0832D>.
- [12] P. Stavroulakis, C.L. Freeman, D. Patel, C. Utton, R. Goodall, Successful prediction of the elastic properties of multiphase high entropy alloys in the AlTiVCr-Si system through a novel computational approach, *Materialia* 21 (2022), 101365, <https://doi.org/10.1016/j.mtla.2022.101365>, February.
- [13] R. Feng, et al., Elastic behavior of binary and ternary refractory multi-principal-element alloys, *Mater. Des.* 219 (2022), 110820, <https://doi.org/10.1016/j.matdes.2022.110820>.
- [14] M. Sarwan, A. Shukoor V, F. Shareef M, S. Singh, A first principle study of structural, elastic, electronic and thermodynamic properties of Half-Heusler compounds; YNiPn (Pn=As, sb, and bi), *Solid State Sci.* 112 (2021), 106507, <https://doi.org/10.1016/j.solidstatosciences.2020.106507>.
- [15] M. Yang, L. Shao, J.M. Duan, X.T. Chen, B.Y. Tang, Temperature dependence of mechanical and thermodynamic properties of Ti(25+x)Zr25Nb25Ta(25-x) (x ≤ 20) refractory high entropy alloys: influences of substitution of Ti for Ta, *Phys. B Condens. Matter* 606 (November 2020), 412851, <https://doi.org/10.1016/j.physb.2021.412851>, 2021.
- [16] J. Zhang, C. Cai, G. Kim, Y. Wang, W. Chen, Composition design of high-entropy alloys with deep sets learning, *npj Comput. Mater.* 2022 8 (1) (Apr. 2022) 1–11, <https://doi.org/10.1038/s41524-022-00779-7>.
- [17] S. Qiu, S.M. Chen, N. Naihua, J. Zhou, Q.M. Hu, Z. Sun, Structural stability and mechanical properties of B2 ordered refractory AlNbTiVZr high entropy alloys, *J. Alloys Compd.* 886 (2021), 161289, <https://doi.org/10.1016/j.jallcom.2021.161289>.
- [18] Y. Zhao, H. Li, Y. Huang, The structure, mechanical, electronic and thermodynamic properties of bcc Zr-Nb alloy: a first principles study, *J. Alloys Compd.* 862 (2021), 158029, <https://doi.org/10.1016/j.jallcom.2020.158029>.
- [19] H. Song, Q. Ma, W. Zhang, F. Tian, Effects of vacancy on the thermodynamic properties of Co-Cr-Fe-Mn-Ni high-entropy alloys, *J. Alloys Compd.* 885 (2021), 160944, <https://doi.org/10.1016/j.jallcom.2021.160944>.
- [20] C. Chang, H. Zhang, First-principles calculations to investigate elastic and thermodynamic properties of FeAlNiCrMn quaternary alloys, *J. Mater. Res. Technol.* 18 (May 2022) 1322–1332, <https://doi.org/10.1016/j.jmrt.2022.03.046>.
- [21] Y. Chen, Q. Zhao, H. Wu, Q. Fang, J. Li, Effect of interstitial N atom on physical and mechanical properties of FeCoCrNiMn high-entropy alloys: a first-principles study, *Phys. B Condens. Matter* 615 (April) (2021), 413078, <https://doi.org/10.1016/j.physb.2021.413078>.
- [22] H. Liu, L. Liu, C. Xin, Effect of alloying elements on the structure and mechanical properties of NbMoTaWX (X = Cr, V, Ti, Zr, and Hf) refractory high-entropy alloys, *AIP Adv.* 11 (2) (2021), <https://doi.org/10.1063/5.0038405>.
- [23] J. Hu, et al., The effect of hydrogen on the mechanical properties of high entropy alloy TiZrHfNbNb: first-principles investigation, *J. Alloys Compd.* 879 (2021), 160482, <https://doi.org/10.1016/j.jallcom.2021.160482>.
- [24] U. Bhandari, H. Ghadimi, C. Zhang, F. Gao, S. Yang, S. Guo, Computational exploration of biomedical HfNbTaTiZr and Hf0.5Nb0.5Ta0.5Ti1.5Zr refractory high-entropy alloys, *Mater. Res. Express* 8 (9) (Sep. 2021), <https://doi.org/10.1088/2053-1591/AC1D65>.
- [25] C. Li, Y. Ma, X. Yang, M. Hou, New TiTaNbZrMo high-entropy alloys for metallic biomaterials, *Mater. Res. Express* 8 (10) (2021), <https://doi.org/10.1088/2053-1591/ac2f0b>.
- [26] L. Shao, M. Yang, L. Ma, B.Y. Tang, Effect of Ta and Ti content on high temperature elasticity of HfNbZrTa1–xTix refractory high-entropy alloys, *Int. J. Refract. Met. Hard Mater.* 95 (2021), <https://doi.org/10.1016/j.ijrmhm.2020.105451>.
- [27] G. Hayashi, K. Suzuki, T. Terai, H. Fujii, M. Ogura, K. Sato, Prediction model of elastic constants of BCC high-entropy alloys based on first-principles calculations and machine learning techniques, *SSRN Electron. J.* (2022), <https://doi.org/10.2139/ssrn.3994455>.
- [28] N.D. Tran, A. Saengdeejing, K. Suzuki, H. Miura, Y. Chen, Stability and thermodynamics properties of CrFeNiCoMn/Pd high entropy alloys from first principles, *J. Phase Equilibria Diffus.* 42 (5) (2021) 606–616, <https://doi.org/10.1007/s11669-021-00900-1>.
- [29] S. San, Y. Tong, H. Bei, B. Komabaiah, Y. Zhang, W.Y. Ching, First-principles calculation of lattice distortions in four single phase high entropy alloys with experimental validation, *Mater. Des.* 209 (2021), 110071, <https://doi.org/10.1016/j.matdes.2021.110071>.
- [30] N.D. Tran, T. Davey, Y. Chen, DFT calculations of structural, magnetic, and stability of FeNiCo-based and FeNiCr-based quaternary alloys, *J. Appl. Phys.* 133 (4) (2023), <https://doi.org/10.1063/5.0134915>.
- [31] I. Lobzenko, D. Wei, M. Itakura, Y. Shiihara, T. Tsuru, Improved mechanical properties of Co-free high-entropy Cantor alloy: a first-principles study, *Results Mater.* 17 (November 2022), 100364, <https://doi.org/10.1016/j.rimma.2023.100364>, 2023.
- [32] E.P. George, D. Raabe, R.O. Ritchie, High-entropy alloys, *Nat. Rev. Mater.* 2019 48 (4) (Jun. 2019) 515–534, <https://doi.org/10.1038/s41578-019-0121-4>.
- [33] R. Wei, et al., Novel Co-free high performance TRIP and TWIP medium-entropy alloys at cryo[1], *Mater. Sci. Eng. A*, vol. 764, p. 138212, in: M. Zhang, L. Zhang, J. Fan, P. Yu, G. Li (Eds.), *Novel Co-free CrFeNiNb0.1Tix High-Entropy Alloys with Ultra High Hardness and Strength*, vol. 57, Nov. 2020, pp. 153–158, <https://doi.org/10.1016/J.JMST.2020.05.010>.
- [34] Y.L. Zhao, et al., Development of high-strength Co-free high-entropy alloys hardened by nanosized precipitates, *Scripta Mater.* 148 (Apr. 2018) 51–55, <https://doi.org/10.1016/J.SCRIPTAMAT.2018.01.028>.
- [35] Y. Yin, et al., Novel cost-effective Fe-based high entropy alloys with balanced strength and ductility, *Mater. Des.* 162 (Jan. 2019) 24–33, <https://doi.org/10.1016/j.matdes.2018.11.033>.
- [36] M. Zhang, L. Zhang, J. Fan, P. Yu, G. Li, Novel Co-free CrFeNiNb0.1Tix high-entropy alloys with ultra high hardness and strength, *Mater. Sci. Eng., A* 764 (Sep. 2019), 138212, <https://doi.org/10.1016/J.MSEA.2019.138212>.
- [37] R.K. Nutor, M. Azeemullah, Q.P. Cao, X.D. Wang, D.X. Zhang, J.Z. Jiang, Microstructure and properties of a Co-free Fe50Mn27Ni10Cr13 high entropy alloy, *J. Alloys Compd.* 851 (Jan. 2021), 156842, <https://doi.org/10.1016/j.jallcom.2020.156842>.
- [38] A. Verma, et al., High temperature wear in CoCrFeNiCu high entropy alloys: the role of Cu, *Scripta Mater.* 161 (Mar. 2019) 28–31, <https://doi.org/10.1016/J.SCRIPTAMAT.2018.10.007>.
- [39] Y. Yu, et al., A novel Cu-doped high entropy alloy with excellent comprehensive performances for marine application, *J. Mater. Sci. Technol.* (2020), <https://doi.org/10.1016/j.jmst.2020.08.016>.
- [40] K.N. Campo, C.C. de Freitas, E.B. da Fonseca, R. Caram, CrCuFeMnNi high-entropy alloys for semisolid processing: the effect of copper on phase formation, melting

- behavior, and semisolid microstructure, *Mater. Charact.* 178 (Aug. 2021), 111260, <https://doi.org/10.1016/J.MATCHAR.2021.111260>.
- [41] C. Li, J.C. Li, M. Zhao, Q. Jiang, Effect of alloying elements on microstructure and properties of multiprincipal elements high-entropy alloys, *J. Alloys Compd.* 475 (1–2) (May 2009) 752–757, <https://doi.org/10.1016/j.jallcom.2008.07.124>.
- [42] B. Ren, Z.X. Liu, D.M. Li, L. Shi, B. Cai, M.X. Wang, Effect of elemental interaction on microstructure of CuCrFeNiMn high entropy alloy system, *J. Alloys Compd.* 493 (1–2) (Mar. 2010) 148–153, <https://doi.org/10.1016/j.jallcom.2009.12.183>.
- [43] S.M. Oh, S.I. Hong, Microstructural stability and mechanical properties of equiatomic CoCrCuFeNi, CrCuFeMnNi, CoCrCuFeMn alloys, *Mater. Chem. Phys.* 210 (May 2018) 120–125, <https://doi.org/10.1016/j.matchemphys.2017.09.010>.
- [44] R.F. Zhao, B. Ren, G.P. Zhang, Z.X. Liu, J.J. Zhang, Phase transition of as-milled and annealed CrCuFeMnNi high-entropy alloy, *Powder* 13 (9) (2018), <https://doi.org/10.1142/S179329201850100X>.
- [45] A. Shabani, M.R. Toroghinejad, M. Aminaei, Effect of prior cold deformation on recrystallization behavior of a multi-phase FeCrCuMnNi high entropy alloy, *Mater. Chem. Phys.* 272 (Nov. 2021), 124991.
- [46] A. Shabani, M.R. Toroghinejad, Investigation of microstructure, texture, and mechanical properties of a FeCrCuMnNi multiphase high entropy alloy during recrystallization, *Mater. Charact.* 154 (April) (Aug. 2019) 253–263, <https://doi.org/10.1016/j.matchar.2019.05.043>.
- [47] A. Shabani, M.R. Toroghinejad, A. Shafyei, P. Cavaliere, Effect of cold-rolling on microstructure, texture and mechanical properties of an equiatomic FeCrCuMnNi high entropy alloy, *Materialia* 1 (Sep. 2018) 175–184, <https://doi.org/10.1016/j.mtla.2018.06.004>.
- [48] A. Shabani, M.R. Toroghinejad, A. Shafyei, R.E. Logé, Microstructure and mechanical properties of a multiphase FeCrCuMnNi high-entropy alloy, *J. Mater. Eng. Perform.* 28 (4) (Apr. 2019) 2388–2398, <https://doi.org/10.1007/s11665-019-04003-4>.
- [49] T.P.C. Klaver, D. Simonovic, M.H.F. Sluiter, Brute force composition scanning with a CALPHAD database to find low temperature body centered Cubic High Entropy alloys, *Entropy* 20 (2018) 12, <https://doi.org/10.3390/e20120911>.
- [50] P. Giannozzi, et al., Quantum espresso: a modular and open-source software project for quantum simulations of materials, *J. Phys. Condens. Matter* 21 (39) (2009), <https://doi.org/10.1088/0953-8984/21/39/395502>.
- [51] J.P. Perdew, K. Burke, M. Ernzerhof, Generalized gradient approximation made simple 77 (18) (1996) 3865–3868.
- [52] M.T. McClellan, J. Minker, D.E. Knuth, “The art of computer programming, Math. Comput., vol. 28, in: Sorting and Searching, vol. 3, 1974, p. 128, <https://doi.org/10.2307/2005383>.
- [53] U. Bhandari, C. Zhang, S. Yang, Mechanical and thermal properties of low-density Al_{20+x}Cr_{20-x}Mo_{20-y}Ti₂₀V_{20+y} Alloys, *Crystals* 10 (4) (2020), <https://doi.org/10.3390/cryst10040278>.
- [54] U. Bhandari, C. Zhang, C. Zeng, S. Guo, S. Yang, Computational and experimental investigation of refractory high entropy alloy mo15nb20re15ta30w20, *J. Mater. Res. Technol.* 9 (4) (2020) 8929–8936, <https://doi.org/10.1016/J.JMRT.2020.06.036>.
- [55] U. Bhandari, C. Zhang, S. Guo, S. Yang, First-principles study on the mechanical and thermodynamic properties of MoNbTaTiW, *Int. J. Miner. Metall. Mater.* 27 (10) (2020), <https://doi.org/10.1007/s12613-020-2077-1>.
- [56] O.L. Anderson, A simplified method for calculating the debye temperature from elastic constants, *J. Phys. Chem. Solid.* 24 (7) (1963) 909–917, [https://doi.org/10.1016/0022-3697\(63\)90067-2](https://doi.org/10.1016/0022-3697(63)90067-2).
- [57] K.W. Andrews, Elastic moduli of polycrystalline cubic metals, *J. Phys. Appl. Phys.* 11 (18) (1978) 2527–2534, <https://doi.org/10.1088/0022-3727/11/18/011>.
- [58] Thermische eigenschaften der Stoffe, Thermische Eig. der Stoffe (1926), <https://doi.org/10.1007/978-3-642-99531-6>.
- [59] B. Mayer, et al., Ab-initio calculation of the elastic constants and thermal expansion coefficients of Laves phases, *Intermetallics* 11 (2003) 1, [https://doi.org/10.1016/S0966-9795\(02\)00127-9](https://doi.org/10.1016/S0966-9795(02)00127-9).
- [60] ASTM E228-17, Standard Test Method for Linear Thermal Expansion of Solid Materials With a Push-Rod Dilatometer, 14, ASTM International, 2018, pp. 1–10.
- [61] ASTM E1269-11, Standard Test Method for Determining Specific Heat Capacity by Differential Scanning Calorimetry, 14, ASTM International, 2018, pp. 1–6.
- [62] ASTM E1876-22, Standard Test Method for Dynamic Young's Modulus, Shear Modulus, and Poisson's Ratio by Impulse Excitation of Vibration, ASTM International 03 (01) (2022) 1–19.
- [63] S. Spinner, T.W. Reichard, W.E. Tefft, A comparison of experimental and theoretical relations between Young's modulus and the flexural and longitudinal resonance frequencies of uniform bars, *J. Res. Natl. Bur. Stand. Sect. A, Phys. Chem.* 64A (2) (Mar. 1960) 147, <https://doi.org/10.6028/JRES.064A.014>.
- [64] F. Adel, S. Shokrollahi, E. Beygi, Determination of Young's Modulus by Finite Element Model Updating, *Modares Mechanical Engineering* 19 (8) (August 2019) 1837–1844.
- [65] S. Mukhanov, P. Loginov, A. Fedotov, M. Bychkova, M. Antonyuk, E. Levashov, The effect of copper on the microstructure, wear and corrosion resistance of CoCrCuFeNi high-entropy alloys manufactured by powder metallurgy, *Mater.* 2023 16 (3) (Jan. 2023) 1178, <https://doi.org/10.3390/MA16031178>, 16, Page 1178.
- [66] L. Huang, X. Wang, B. Huang, X. Zhao, H. Chen, C. Wang, Effect of Cu segregation on the phase transformation and properties of AlCrFeNiTiCux high-entropy alloys, *Intermetallics* 140 (Jan. 2022), 107397, <https://doi.org/10.1016/J.INTERMET.2021.107397>.
- [67] Y. Cai, Y. Chen, Z. Luo, F. Gao, L. Li, Manufacturing of FeCoCrNiCux medium-entropy alloy coating using laser cladding technology, *Mater. Des.* 133 (Nov. 2017) 91–108, <https://doi.org/10.1016/J.IJMATES.2017.07.045>.
- [68] S.F. Pugh, XCII. Relations between the elastic moduli and the plastic properties of polycrystalline pure metals, London, Edinburgh Dublin Phil. Mag. J. Sci. 45 (1954) 367, <https://doi.org/10.1080/14786440808520496>.
- [69] D.G. Pettifor, Theoretical predictions of structure and related properties of intermetallics, *Mater. Sci. Technol.* 8 (1992) 4, <https://doi.org/10.1179/mst.1992.8.4.345>.
- [70] G. Kim, et al., First-principles and machine learning predictions of elasticity in severely lattice-distorted high-entropy alloys with experimental validation, *Acta Mater.* 181 (Dec. 2019) 124–138, <https://doi.org/10.1016/J.ACTAMAT.2019.09.026>.
- [71] W. Hermann, H.-G. Sockel, K.L. Edwards, Elastic modulus measurement, *Ref. Modul. Mater. Eng.* 98 (2016), <https://doi.org/10.1016/b978-0-12-803581-8.03417-2>.
- [72] K. Tanaka, T. Teramoto, R. Ito, Monocrystalline elastic constants of fcc-CrMnFeCoNi high entropy alloy, *MRS Adv.* 2 (27) (Jan. 2017) 1429–1434, <https://doi.org/10.1557/ADV.2017.76/METRICS>.
- [73] A. Haglund, M. Koehler, D. Catoor, E.P. George, V. Keppens, Polycrystalline elastic moduli of a high-entropy alloy at cryogenic temperatures, *Intermetallics* 58 (Mar. 2015) 62–64, <https://doi.org/10.1016/J.INTERMET.2014.11.005>.
- [74] F. Tian, L.K. Varga, J. Shen, L. Vitos, Calculating elastic constants in high-entropy alloys using the coherent potential approximation: current issues and errors, *Comput. Mater. Sci.* 111 (Jan. 2016) 350–358, <https://doi.org/10.1016/J.COMMATSCI.2015.09.058>.
- [75] Z. Wu, H. Bei, G.M. Pharr, E.P. George, Temperature dependence of the mechanical properties of equiatomic solid solution alloys with face-centered cubic crystal structures, *Acta Mater.* 81 (2014) 428–441, <https://doi.org/10.1016/J.ACTAMAT.2014.08.026>.
- [76] S. Gorsse, M.H. Nguyen, O.N. Senkov, D.B. Miracle, Database on the mechanical properties of high entropy alloys and complex concentrated alloys, *Data Brief* 21 (Dec. 2018) 2664–2678, <https://doi.org/10.1016/j.dib.2018.11.111>.
- [77] A. Shabani, M.R. Toroghinejad, Investigation of the Microstructure and the Mechanical Properties of Cu-NiC Composite Produced by Accumulative Roll Bonding and Coating Processes 24 (12) (Dec. 2015) 4746–4754.
- [78] A. Shabani, M.R. Toroghinejad, A. Shafyei, Fabrication of Al/Ni/Cu composite by accumulative roll bonding and electroplating processes and investigation of its microstructure and mechanical properties, *Mater. Sci. Eng., A* 558 (Dec. 2012) 386–393.